

High Resolution Simulation and Characterization of Density-Driven Flow in CO₂ Storage in Saline Aquifers

George S. H. Pau*, John B. Bell, Karsten Pruess, Ann S. Almgren, Michael J. Lijewski, Keni Zhang

Lawrence Berkeley National Laboratory, 1 Cyclotron Road, Berkeley, CA 94720

Abstract

Simulations are routinely used to study the process of carbon dioxide (CO₂) sequestration in saline aquifers. In this paper, we describe the modeling and simulation of the dissolution-diffusion-convection process based on a total velocity splitting formulation for a variable-density incompressible single-phase model. A second-order accurate sequential algorithm, implemented within a block-structured adaptive mesh refinement (AMR) framework, is used to perform high resolution studies of the process. We study both the short term and long term behaviors of the process. It is found that the onset time of convection follows closely the prediction of linear stability analysis. In addition, the CO₂ flux at the top boundary, which gives the rate at which CO₂ gas dissolves into a negatively buoyant aqueous phase, will reach a stabilized state at the space and time scales we are interested in. This flux is found to be proportional to permeability, and independent of porosity and effective diffusivity, indicative of a convection-dominated flow. A 3D simulation further shows that the added degrees of freedom shorten the onset time and increase the magnitude of the stabilized CO₂ flux by about 25%. Finally, our results are found to be comparable to results obtained from TOUGH2-MP.

1. Introduction

Geologic carbon dioxide (CO₂) sequestration involves injecting CO₂ into saline aquifers. The primary mechanism of securing the CO₂ relies on a leak-proof formation to prevent the immiscible CO₂ gas that forms on top of the brine from leaking to the surface. However, on geological time scales, secondary geochemical mechanisms, such as dissolution trapping and mineral trapping can play significant roles [11] by either changing the CO₂ into a negatively buoyant state or immobilizing the CO₂. Dissolution trapping occurs when CO₂ dissolves into the brine under ambient temperature and pressure conditions in a typical aquifer. This increases the density of the brine at the interface of the layers by 0.1-1%, depending on the salinity of the brine. Due to the gravitational instability and the heterogeneity in the rock properties of the aquifer, CO₂-rich brine fingers will form, leading to a convective flow that transports these CO₂-rich brines downward while driving brine with low CO₂ concentration upwards. This mechanism accelerates the rate at which CO₂ is dissolved and provides a more secure mechanism by which CO₂ can be stored [4, 20, 27]. In this work, we focus on the dissolution-diffusion-convection process. We do not consider the effects of mineral trapping on the process, although they can be significant [3, 11].

*Corresponding author. Tel.: +1 510 486 7196; fax: +1 510 486 6900.

The significance of density change due to dissolution of CO₂ in the context of CO₂ storage was first proposed by Weir and his coworkers [24, 25]. Lindeberg and Wessel-Berg [14] then studied the stability criteria for the dissolution-diffusion-convection process. This is followed by several linear stability analyses [4, 5, 7, 22, 26] that yield important relations for the onset time for convection, the dominant wavelength for growth of convective plumes and the growth rates of these fingers. Results from these analyses are also found to be consistent with results from high-accuracy direct numerical simulations [22]. In these studies, the formation properties are usually assumed to be homogeneous (except in [4, 5] where anisotropic permeability fields are considered), and perturbations are introduced directly into the initial concentration profile. In addition, the incompressibility and Boussinesq assumptions are made.

There are fewer theoretical studies on the effects of heterogeneity on the onset of convection and the subsequent convective behavior. Gounot and Caltagirone [6] attempted to model the effects of fluctuation in permeability on free convection. However, the prevalent approach of studying the effects of heterogeneity is through direct numerical simulations. Numerical studies using TOUGH family of codes by Pruess and Zhang [20] suggested that relations derived from linear stability analyses are valid. In their studies, a full compressible model with detailed equation of states is used although the simulations are limited by the achievable grid resolution.

Accurate characterization of the long term behavior of the convective process is also important. Riaz et al. [22] showed that the long term behavior of the flow cannot be predicted from the initial concentration profiles based on the linear stability analysis, especially for large Rayleigh numbers. Further examinations of the long term behavior of the CO₂ flux [7, 20] suggested that the dissolution rate fluctuates about a constant mean value. Results in [20] suggested that this mean dissolution rate is approximately 1.5 – 2 times larger than the dissolution rate at the onset of convection. The contribution of the convective process towards enhancing the dissolution rate is thus significant considering the fact that the dissolution rate is a function of $\sqrt{1/t}$ in the absence of convective process [20]. Laboratory studies [12, 27] have so far obtained results that are qualitatively and quantitatively similar to the simulation results.

We note that the dissolution-diffusion-convection process is conceptually similar to unsteady thermal boundary layer problem. Existing literature (e.g. [16, 21] and references therein) on the unstable thermal boundary-layer problem adds to our understanding of the dissolution-diffusion-convection process. However, as pointed out in [8, 20], there are important differences. In a geothermal problem, the initial condition is usually given by a constant temperature gradient while in the CO₂ dissolution problem, no initial gradient of dissolved aqueous CO₂ exists, resulting in a system that is unconditionally unstable for buoyancy-driven convection [20]. In addition, the change in the density in the current problem must be accounted for through a mass flux boundary condition [8, 9] so that the mass balance law is observed. In thermal problems, a Dirichlet boundary condition is usually used. We note that most linear stability analyses utilize the latter form of boundary condition.

The goal of this work is to use high-resolution simulations to accurately characterize the dissolution-diffusion-convection process. We use a variable-density incompressible single-phase model, described in Section 2, that takes into consideration the compositional effects on density and allows us to study the effects of the heterogeneity in the permeability on the onset of instability. Thus, it is different from models in previous studies that use the Boussinesq approximation. The Boussinesq approximation also necessitates the use of either a perturbed

Fluid properties	
viscosity, μ	0.5947×10^{-3} Pas
water density, ρ_w	994.56 kgm^{-3}
saturated CO ₂ mass fraction, X_1	0.049306
density increase due to CO ₂ dissolution, $\Delta\rho$	10.45 kgm^{-3}
diffusivity, \mathcal{D}	$2 \times 10^{-9} \text{ m}^2\text{s}^{-1}$ [23]

Table 1: Fluid properties.

initial condition [22] or a randomized porosity distribution to initiate the instability. We elaborate further on this in Section 2.2. We then solve the resulting system of equations using a parallelized second-order accurate block-structured adaptive method described in Section 3. Compared to other existing numerical studies, such as [4, 20], our numerical approach allows tight control of numerical errors and numerical dispersion. In addition, the adaptive mesh refinement framework allows us to capture the small scale dynamics that have significant influence on the large scale fingering structure and late time behavior [22]. In Section 4, we examine the onset of convection and the long-term behavior of the diffusion-convection process. In particular, we examine how the onset time of convection and the long-term stabilized mass flux vary with permeability, porosity, and effective diffusivity. These numerical results are preceded by some discussions of the numerical aspects of simulating the two stages of the process. Although most of the analyses are based on 2D models, we also examine a full 3D problem based on hydrogeologic parameters appropriate for the Carrizo-Wilcox aquifer in Texas [15]. In Section 5, some of the results are compared to those obtained through TOUGH2-MP, a parallelized version of the general-purpose simulator TOUGH2/ECO2N [18, 19, 28]. We conclude by proposing a 1D model for simulating the dissolution-diffusion-convection process at field scale in Section 6.

2. Problem Formulation

2.1. Setup

Figure 1 shows the simulation setup for a two dimensional problem. The simulation domain, of height H and width W , is impermeable to fluid flow on the top and bottom boundaries and is periodic on left and right boundaries. The CO₂-saturated brine forms a separate layer above the impermeable top boundary; we assume the dissolution rate of CO₂ gas into the layer is sufficiently high that the layer remains saturated for the length of the simulation. We allow diffusion of CO₂-saturated brine into the simulation domain through the top boundary. This simulation setup then allows us to use a variable-density single-phase incompressible model to treat the dissolution-diffusion-convection process.

The fluid properties, as specified in Table 1, are derived from the ECO2N fluid module of TOUGH2 [19] and correspond to pure water (no salinity) at temperature and pressure conditions of $T = 45^\circ\text{C}$, $P = 100$ bar, as would be encountered in typical terrestrial crust near 1000 m depth. Isothermal conditions are assumed.

2.2. Governing Equations

The mass conservation equations are given by

$$\frac{\partial \phi \rho X_\alpha}{\partial t} + \nabla \cdot (\rho X_\alpha \mathbf{u}) = \nabla \cdot \phi \tau \mathcal{D} \rho \nabla X_\alpha, \quad \alpha = 1, 2 \quad (1)$$

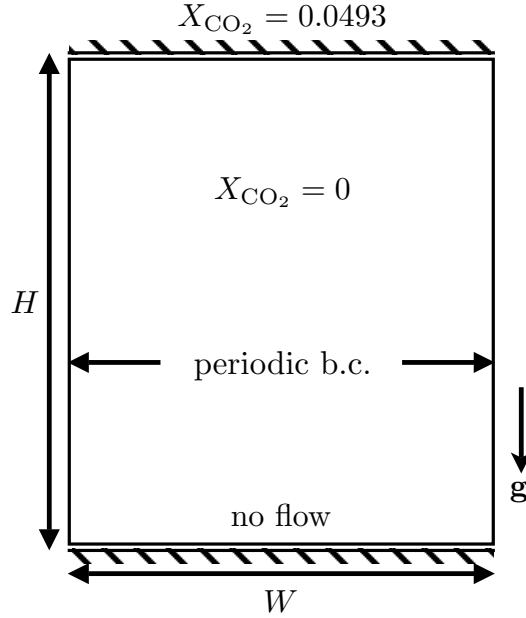


Figure 1: Setup

where X_1 is the mass fraction of CO_2 , X_2 is the mass fraction of water, ρ is the density of the aqueous phase, τ is the tortuosity coefficient, \mathcal{D} is the diffusion coefficient, and ϕ is the porosity coefficient. The term $\tau\mathcal{D}$ is also known as the effective diffusivity. The volumetric flux \mathbf{u} is given by Darcy's law:

$$\mathbf{u} = -\frac{\kappa}{\mu}(\nabla p - \rho\mathbf{g}). \quad (2)$$

The system is closed by the equation of state given by

$$\rho \left(\frac{X_1}{\rho_1} + \frac{X_2}{\rho_2} \right) = 1, \quad (3)$$

where ρ_1 is the density of saturated aqueous CO_2 and ρ_2 is the density of water. The equation of state reflects the condition that there is no volume change upon mixing. We note that by summing (1) over all the components, we obtain

$$\frac{\partial \phi \rho}{\partial t} + \nabla \cdot (\rho \mathbf{u}) = 0, \quad (4)$$

For this system, we want to understand how the equation of state constrains its evolution. In particular, we want to relate the equation of state to a condition on the velocity divergence. This will then allow us to derive a pressure equation for use in our sequential numerical scheme described in Section 3. We first define

$$\mathbf{D}_\phi = \phi \frac{\partial}{\partial t} + \mathbf{u} \cdot \nabla, \quad (5)$$

which is a scaled Lagrangian derivative. Then, (1) and (4) can be expressed as

$$\rho \mathbf{D}_\phi X_1 = \nabla \cdot \phi \tau \mathcal{D} \rho \nabla X_1, \quad (6)$$

$$\mathbf{D}_\phi \rho + \rho \nabla \cdot \mathbf{u} = 0. \quad (7)$$

If we apply \mathbf{D}_ϕ to (3), we obtain

$$\frac{1}{\rho} \mathbf{D}_\phi \rho + \sum_{\alpha=1}^2 \frac{\rho}{\rho_\alpha} \mathbf{D}_\phi X_\alpha = 0. \quad (8)$$

By substituting (6) and (7) into the above, we obtain

$$\nabla \cdot \mathbf{u} = \sum_{\alpha=1}^2 \frac{1}{\rho_\alpha} \nabla \cdot \phi \rho \tau \mathcal{D} \nabla X_\alpha. \quad (9)$$

Similar results are obtained in [2]. A similar compressible model can be found in [8].

Substituting (2) into (9), we obtain an elliptic equation given by

$$-\nabla \cdot \frac{\kappa}{\mu} (\nabla p - \rho \mathbf{g}) = \sum_{\alpha=1}^2 \frac{1}{\rho_i} \nabla \cdot \phi \rho \tau \mathcal{D} \nabla X_\alpha. \quad (10)$$

We impose no flow boundary condition on the bottom boundary; $-\frac{\kappa}{\mu} \nabla p = \sum_{\alpha=1}^2 \frac{1}{\rho_\alpha} \rho \tau \mathcal{D} \nabla X_\alpha$ on the top boundary; and periodic boundary conditions in all other directions.

Let us point out one difference between models with and without the Boussinesq approximation that is relevant to the current work. With the Boussinesq approximation, the pressure equation is given by

$$-\nabla \cdot \frac{\kappa}{\mu} (\nabla p - \rho \mathbf{g}) = 0. \quad (11)$$

Let us assume the density ρ is initially uniform in the simulation domain. At time $t > 0$, CO_2 enters the domain only through diffusion. With uniform ϕ and τ , the change in X_1 , the mass fraction of CO_2 , is independent of the horizontal coordinate. This generates a change in ρ that is also independent of the horizontal coordinate. Since $\rho \mathbf{g}$ is now independent of the horizontal coordinate, (11) is solved by

$$p = p_0 + \int_{-y}^0 \rho(y') \mathbf{g} dy', \quad (12)$$

where y denotes the coordinate in the vertical direction. The above implies that the velocity is identically zero, and thus does not depend on the variation in κ . Fluctuations in κ alone cannot induce convective instability in the flow. The instability must then be initiated by introducing fluctuations in the porosity or the initial concentration profile. For our model, a gradient in X introduces a nonzero RHS in (10), leading to variation in pressure p and a nonzero velocity \mathbf{u} that are dependent on κ . Thus, fluctuations in κ will eventually lead to instability, allowing us to examine the effects of the fluctuations in κ on the onset of convection and its subsequent behavior. Within the incompressible framework, the model we presented is exact in the sense that it takes the compositional effects on density into full consideration. In addition, it does not add much computational cost to a simulation based on a model that employs the Boussinesq approximation. Other consequences of applying the Boussinesq assumption are documented in [8, 10, 13].

3. Numerical Method

The basic integration scheme is based on the total velocity approach. Component equations (1) and the pressure equation (10) form a set of coupled equations that can be efficiently

solved by an IMPES-like method in which the pressure equation is solved implicitly and the mass conservation equations are solved using an explicit treatment of advection and an implicit treatment of diffusion. The basic algorithm is constructed so that the overall splitting approach is second-order accurate in time. The diffusion terms are discretized implicitly so that the diffusive term $\nabla \cdot \phi \rho \tau \mathcal{D} \nabla X$ does not limit the time step so that the time step is controlled by the explicit discretization of advection. We summarize the discretization and time-stepping procedure for a single grid.

The spatial discretization uses a volume of fluid approach in which $(\rho X_\alpha)_{ijk}^n$ denotes the average value of ρX_α over cell (i, j, k) at time t^n ; X_α and p are defined on cell centers while $F_\alpha = \rho X_\alpha \mathbf{u}$ and \mathbf{u} are defined on cell edges. To simplify notation, let $\lambda = \kappa/\mu$. The time stepping procedure is then given as follows.

- **Step 1:** Solve the discretized pressure equation (10), given by

$$\mathbf{D}\lambda(\mathbf{G}p) = \mathbf{D}\lambda\rho\mathbf{g} - \mathbf{D}\sum_{\alpha=1}^2 \frac{1}{\rho_\alpha} \phi \rho \tau \mathcal{D}(\mathbf{G}X_\alpha), \quad (13)$$

for p with properties evaluated using ρ^n and X^n . We then use equation (2) to define the Darcy velocity \mathbf{u}^n . Here \mathbf{D} and \mathbf{G} are second-order accurate discretizations of the divergence and gradient operators, respectively. The divergence operator returns a cell-centered divergence from face-centered values; the gradient operator differences cell-centered values to return normal gradients on faces. In two dimensions the discretization of $\mathbf{D}\lambda(\mathbf{G}p)$ at cell (i, j) would be

$$\frac{\lambda_{i+\frac{1}{2},j}(p_{i+1,j} - p_{i,j}) - \lambda_{i-\frac{1}{2},j}(p_{i,j} - p_{i-1,j})}{\Delta x^2} + \frac{\lambda_{i,j+\frac{1}{2}}(p_{i,j+1} - p_{i,j}) - \lambda_{i,j-\frac{1}{2}}(p_{i,j} - p_{i,j-1})}{\Delta y^2}$$

where Δx and Δy are the mesh spacings in the x and y directions, respectively. (We note that although we include this initial solution of the pressure equation as formally part of the method, it does not need to be done in practice. See discussion below.)

- **Step 2:** Use (1) to advance the solution from time t^n to time t^{n+1} based on \mathbf{u}^n . We use an unsplit second-order Godunov scheme to compute the hyperbolic fluxes. The Godunov discretization is then coupled to a Crank-Nicolson discretization of the diffusive terms, so that

$$\phi \frac{(\rho X)^{n+1,*} - (\rho X)^n}{\Delta t} + \mathbf{D}F^{n+1/2,*} = \frac{1}{2} \left(\sum_{i=1}^2 \mathbf{D} \frac{1}{\rho_i^n} \phi \rho^n \tau \mathcal{D} \mathbf{G} X^n + \mathbf{D} \frac{1}{\rho_i^{n+1,*}} \phi \rho^{n+1,*} \tau \mathcal{D} \mathbf{G} X^{n+1,*} \right) \quad (14)$$

with a suitable linearization of the coefficients of the diffusion term; here superscript $(n+1,*)$ denotes functions of ρX evaluated at $(\rho X)^{n+1,*}$. In this step, $F^{n+1/2,*}$ denotes time-centered fluxes computed using the Godunov procedure but with the total velocity evaluated at t^n .

- **Step 3:** Solve the pressure equation (9), with properties evaluated using $(\rho X)^{n+1,*}$, to compute a new total Darcy velocity $\mathbf{u}^{n+1,*}$ from (2). We then define $\mathbf{u}^{n+1/2} = \frac{1}{2}(\mathbf{u}^n + \mathbf{u}^{n+1,*})$ so that we can time center the dependence of the flux on \mathbf{u} .

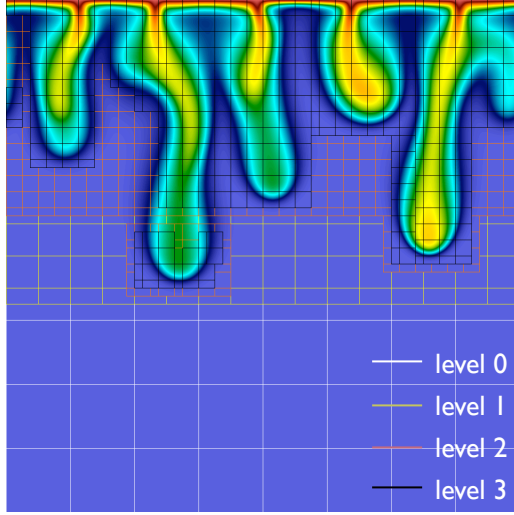


Figure 2: AMR grid with three levels of refinement. Each level of grids is shown with a different color.

- **Step 4:** Use (1) to re-advance the solution from time t^n to time t^{n+1} , this time using $\mathbf{u}^{n+1/2}$ to obtain values of $(\rho X)^{n+1}$,

$$\phi \frac{(\rho X)^{n+1} - (\rho X)^n}{\Delta t} + \mathbf{D}F^{n+1/2} = \frac{1}{2} \left(\sum_{i=1}^2 \mathbf{D} \frac{1}{\rho_i^n} \phi \rho^n \tau \mathcal{D} \mathbf{G} X^n + \mathbf{D} \frac{1}{\rho_i^{n+1}} \phi \rho^{n+1} \tau \mathcal{D} \mathbf{G} X^{n+1} \right) \quad (15)$$

again with a suitable linearization of the coefficients of the diffusion term. In this step, $F^{n+1/2}$ denotes time-centered fluxes computed using the Godunov procedure but with the total velocity evaluated at $t^{n+1/2}$.

In above, $\mathbf{u}^{n+1,*}$ is different from \mathbf{u}^{n+1} , leading, formally, to two pressure solves in each time step. However, numerical studies suggest that the difference between $\mathbf{u}^{n+1,*}$ and \mathbf{u}^{n+1} is sufficiently small that the convergence rate is not adversely affected [17]. We thus use $\mathbf{u}^{n+1,*}$ in lieu of computing \mathbf{u}^{n+1} in Step 1. The overall time-stepping procedure is integrated into an adaptive mesh refinement (AMR) framework to efficiently accommodate the difference in scale between the diffusive boundary layer and the large-scale convective fingers. Details of the algorithm are described in [17]. Our approach to adaptive refinement uses a nested hierarchy of logically rectangular grids with simultaneous refinement of the grids in both space and time. The grid changes with time based on a set of user-defined refinement criteria; we use component density gradients of all the components. Shown in Figure 2 is a snapshot of the grid; finer grids are placed in regions where small features with large concentration gradients are present. The resulting algorithm is parallelized and shows good scaling behavior up to several thousand CPUs (Appendix A).

4. Results

4.1. Onset of Convection

Figure 3 shows a sequence of snapshots of the density of $\text{CO}_{2(\text{aq})}$. They depict the transition from a diffusion-dominated flow to a convection-dominated flow; we note that there is no abrupt change. The slight fluctuations in the diffusive layers, shown in the top snapshot, grow into prominent fingers. These fingers subsequently merge to form larger

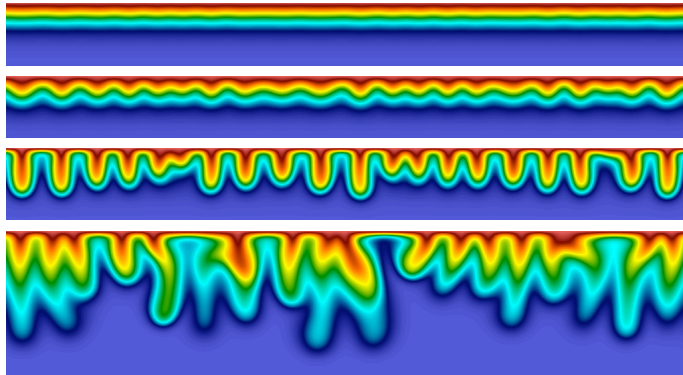


Figure 3: Component density of $\text{CO}_2(\text{aq})$; time increases from top to bottom.

fingers, developing into a more complex flow pattern. The qualitative results shown in Figure 3 are similar to those reported in previous studies [7, 22].

The onset time of convection cannot be defined in an absolute sense. Here, we define the onset time of convection, t_{onset} as the time at which the average mass flux at the top boundary, F_0 , has a relative deviation of 1% from a pure diffusive mass flux and use this definition to determine the time at which convection becomes an important transport mechanism.

During the initial stage of the flow, we are interested in determining the onset time of convection, and how this is affected by the magnitude of and variability in the permeability, porosity and effective diffusivity. The effects are examined directly by creating permeability or porosity distributions with a random fluctuation about a mean value of $\bar{\kappa}$ or $\bar{\phi}$ respectively. In subsequent sections, magnitudes of the mean properties are given by $\bar{\kappa} = 10 \text{ D}$, $\bar{\phi} = 0.3$ and $\tau\mathcal{D} = 2 \times 10^{-9} \text{ m}^2\text{s}^{-1}$, except where noted.

4.1.1. Numerical Considerations

We begin this section with an analysis of the influence of numerical errors on the onset time. For homogeneous permeability and porosity, the two-dimensional problem at hand can be essentially reduced to a one-dimensional diffusion problem. Convective transport is only induced when a non-uniform flow field is generated by the heterogeneity in the permeability or the porosity function. However, linear solvers with finite tolerances can introduce small non-uniform errors that can also eventually lead to instability and convective flow. It is imperative that we ensure that any convective transport in our simulation is induced by the heterogeneity in the formation properties, and not due to the finite tolerances of the linear solver we use. In particular, the tolerances must be sufficiently small that they have limited influence on the dynamics of the flow, and thus the onset time.

Since the Darcy velocity is computed from the pressure gradient, we will look at tolerances of the linear solver used to solve the pressure equation in our numerical scheme. Our multigrid linear solver uses two tolerances to control the accuracy of the linear solve: the relative error tolerance, ε_{rel} and the absolute error tolerance, ε_{abs} . Figure 4 shows that with a uniform $\bar{\kappa} = 10 \text{ D}$ and $\varepsilon_{\text{rel}} = 10^{-12}$, numerical errors will indeed lead to an onset of convection. However, the numerically-induced onset time increases with decreasing ε_{abs} , reflecting the decreasing magnitude of the numerical errors. The numerically-induced onset times are more than a factor of 2 larger than the onset times obtained when 1% fluctuation in κ is introduced. Even then, we note that the onset time converges to a value of $2.3 \times 10^5 \text{ s}$ only when $\varepsilon_{\text{abs}} \leq 10^{-14}$; numerical errors lead to shorter onset times at tolerance levels of

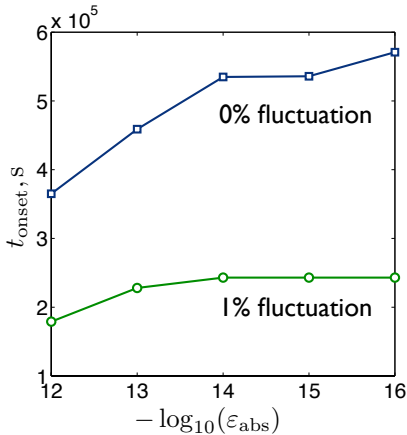


Figure 4: Examining effects of numerical errors on onset time.

$\varepsilon_{\text{abs}} = 10^{-12}$ and 10^{-13} . Decreasing ε_{rel} to 10^{-14} does not change the results. We thus conclude that the convergence criteria given by $\varepsilon_{\text{rel}} = 10^{-12}$ and $\varepsilon_{\text{abs}} = 10^{-14}$ are sufficient to ensure the onset times determined from our simulations are not adversely affected by numerical errors. The above analysis also shows that our method has excellent control of the numerical errors; with appropriate tolerances, we are able to ensure the numerical errors have negligible effects on our simulation.

Another factor that affects the accuracy of the simulation is the grid resolution. Based on linear stability analysis, the dimensional critical wavelength λ_c is defined as [26]

$$\lambda_c = 96.23 \frac{\phi \mu \tau \mathcal{D}}{\kappa \Delta \rho g}. \quad (16)$$

To fully capture the dynamics during the onset of convection, the dimensions of the simulation domain must be significantly larger than λ_c . We ensure that the width is more than 30 times larger than λ_c by varying it with κ , ϕ and \mathcal{D} . In Section 4.2.1, we show that for studying the long term behavior, an even larger width is needed to ensure boundary effect does not distort the evolution of the fingers and to obtain an accurate characterization of the long-term mass flux. The height is chosen such that the finger tips are still sufficiently far from the bottom boundary that the flow is not affected by the bottom boundary. This is similar to the open systems in [7].

The grid resolution must also be sufficiently high to resolve λ_c so that we can capture the initiation of the convective flow accurately. We perform a grid convergence study to determine the appropriate grid size. To ensure the underlying statistics are consistent at different grid resolutions for an uncorrelated random distribution, we adjust the level of fluctuation with grid size. It reflects the notion that for a truly random medium, as grid blocks become larger, the variance of the fluctuations will be lower because of averaging. For example, an initial 1% fluctuation for a given resolution has to be reduced by half when the grid size in each direction is doubled. Experiments confirm that this provides a better convergence behavior.

We examine four grid sizes: $\Delta x = 1/256$, $1/512$, $1/1024$, and $1/2048$. The corresponding fluctuations are given by 0.25%, 0.5%, 1% and 2%. Figure 5 shows that the onset time converges to a single value. From Table 2, we can conclude that the onset time converges to 2.23×10^5 s. An effective resolution of $\Delta x = 1/1024$, which is a factor of 100 smaller than λ_c ,

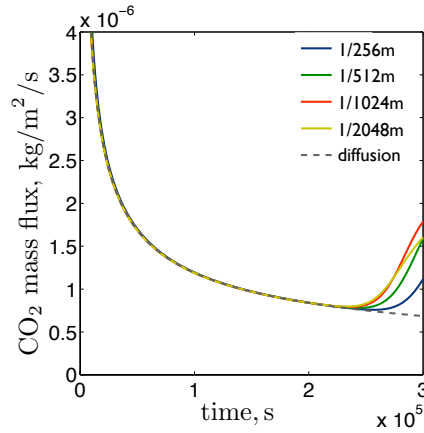


Figure 5: Flux variation at different resolutions. The % fluctuation varies as a function of resolution.

Δx	% fluctuation	onset time, s
1/256	0.25	2.44×10^5
1/512	0.5	2.33×10^5
1/1024	1	2.26×10^5
1/2048	2	2.23×10^5

Table 2: Onset time for different resolutions. The % fluctuation varies as a function of resolution.

is thus sufficient. Results in subsequent sections are obtained based on the tolerances and effective resolution established here.

4.1.2. Onset time

Here, we determine how the onset time varies with the magnitudes of the relative fluctuations in formation properties. We expect the onset time to decrease when the magnitude of the fluctuations is increased. This is indeed borne out by Figure 6. However, Figure 6 further shows that for similar levels of % fluctuation, the fluctuations in ϕ lead to faster onset time than the fluctuations in κ . This is likely because the fluctuations in ϕ cause non-uniform transport of solute from the start of the simulation while the fluctuations in κ require a slow buildup of velocity fluctuations that eventually reach a magnitude that is sufficiently large to induce an onset of convection. Nevertheless, the rates at which the onset times decrease with increasing fluctuation strength are similar.

Linear stability analysis [4] suggests that the onset time is related to properties of the aquifer and fluid through the following relation:

$$t_{\text{onset}} = c_0 \frac{\mu^2 \bar{\phi}^2 \tau \mathcal{D}}{(\Delta \rho)^2 \mathbf{g}^2 \bar{\kappa}^2}. \quad (17)$$

We want to determine whether our simulation results can reproduce the relations between t_{onset} and $\bar{\kappa}$, $\bar{\phi}$ and $\tau \mathcal{D}$ in (17). In the κ case, we vary $\bar{\kappa}$ between 0.01 D and 80 D with a 1% level of fluctuation. Similarly, in the ϕ case, we vary $\bar{\phi}$ between 0.05 and 1, again with 1% fluctuation. In the $\tau \mathcal{D}$ case, $\tau \mathcal{D}$ varies from $0.5 \times 10^{-9} \text{ m}^2 \text{ s}^{-1}$ to $4 \times 10^{-9} \text{ m}^2 \text{ s}^{-1}$. However, $\tau \mathcal{D}$ is uniform and convective behavior is induced by a random κ distribution with a mean of 500 mD and 1% fluctuation with constant $\phi = 0.15$.

Figure 7 clearly shows linear relations between t_{onset} and $1/\bar{\kappa}^2$, $\bar{\phi}^2$, and $\tau \mathcal{D}$ of (17). By determining the gradient of the L_2 -fitted line based on the data for κ , we found c_0 to be

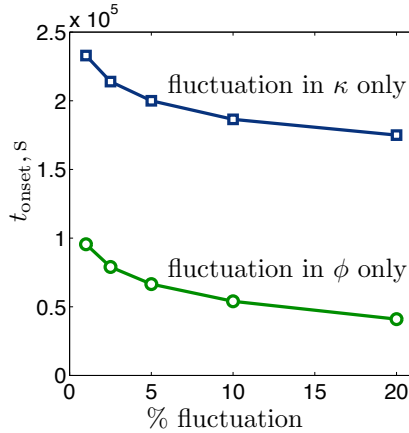


Figure 6: Variation of onset time with % fluctuation in ϕ and % fluctuation in κ .

3670. However, when the same analysis are performed on the data for ϕ , we found c_0 to be 1796. This again shows that for similar levels of fluctuation, the fluctuations in ϕ lead to a shorter onset time. We can also deduce from Figure 6 that c_0 decreases as the % fluctuation increases. We would like to point out that the critical time in [7, 22], which is the onset time in the large Rayleigh number limit [7], is proportional to $\frac{\mu^2 \phi \tau D}{(\Delta \rho)^2 \mathbf{g}^2 \kappa^2}$. This is because the time is scaled by $\phi H^2/D$ instead of H^2/D used by King *et al.* [4, 5] and Xu *et al.* [26]. Our numerical results show that the latter is a more appropriate scaling.

The magnitude of c_0 is of considerable interest and a wide range of values has been reported in the literature. In most cases, the discrepancies can be attributed to different criteria used to define the onset time. In the linear stability analysis performed in [4, 5] that found $c_0 = 75-78$, the onset time is determined by minimizing over all possible wavenumbers the time at which the amplification of the square-averaged perturbation is at its minimum. Using the same criterion, Xu *et al.* [26] obtained a similar value for c_0 . In Riaz *et al.* [22] that reported a value of approximately 500¹, the onset time is defined as the time at which the growth rate of the amplitude of the dominant mode becomes positive within the linear stability analysis framework. Since we use a different definition of onset time, c_0 values we obtained cannot be directly compared to the values obtained in these studies. However, similar to the current paper, Pruess and Zhang [20] define the onset time based on the deviation of a simulated mass flux from a pure diffusive flux, although the % deviation is not specified. They found c_0 to be 1155.6 and 1411.5 for the cases they examined. These values are of the same order of magnitude as our reported values; any discrepancy can be attributed to the differences in the actual % deviation used in defining the onset time, the statistics of the underlying heterogeneity in the rock properties, and the equation of states used in the simulations.

4.2. Long Term Behavior

At long time, the flow is characterized by fingers that extend along the length of the domain, as shown in Figure 8. The velocity field shown in the figure shows pockets of

¹In [22], the onset time relation is given by $t_{\text{onset}} = 146 \frac{\mu^2 \phi \tau D}{(\Delta \rho)^2 \mathbf{g}^2 \kappa^2}$; the exponent of ϕ is 1 instead of 2. Reinterpreting the results in [22], we deduce $c_0 = 487$ and this is consistent with a separate calculation based on Figure 15 of [22] which gives $c_0 = 506$.

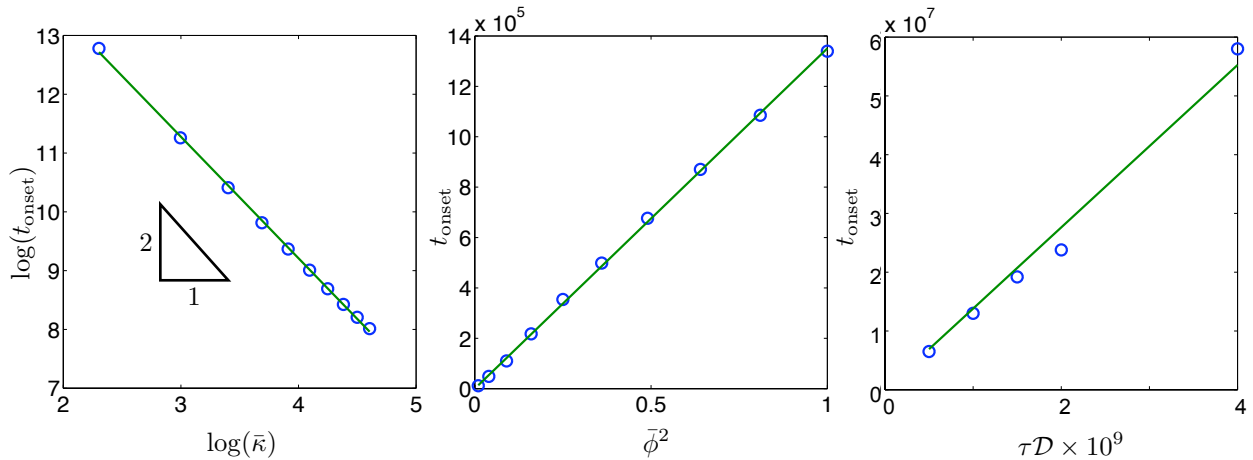


Figure 7: Relations between t_{onset} and $\bar{\kappa}$ (left), $\bar{\phi}^2$ (center), and $\tau\mathcal{D}$ (right). The circles denote the numerically-determined data and the lines represent best linear-fit. The plots clearly show that t_{onset} is proportional to $1/\bar{\kappa}^2$, $\bar{\phi}^2$ and $\tau\mathcal{D}$.

circulating flow: the heavier CO_2 -rich fluid moves downward in distinct fingers while lighter fluid between the fingers moves upward. However, since the top boundary is impermeable, the upward moving solution must move horizontally, pushing nascent fingers into one another and finally into one of the adjacent extended fingers that has a large downward velocity. This indirectly improves the efficiency by which CO_2 is removed from the top boundary. Within an extended finger, we observe that blobs of aqueous CO_2 with higher concentration may pinch off from the extended finger, and move downward at a greater speed. These blobs eventually diffuse to a point where they are indistinguishable from the extended finger. The above descriptions are consistent with the descriptions of the fingering dynamics in [22]. These observations suggest that the dominant mechanism by which CO_2 is transported downward is through the extended fingers that form after the onset of convection.

In [20], Pruess and Zhang concluded that the resulting CO_2 flux will stabilize to a mean value, and fluctuate with a $\pm 15\%$ deviation from the mean. Accurate characterization of this stabilized flux is important as it allows the dissolution-diffusion-convection process to be modeled as a constant flux in a full-scale carbon sequestration simulation. It also determines the rate at which CO_2 is removed from the highly mobile and buoyant gas phase, and put into a less mobile and negatively buoyant aqueous phase. Thus, the quantification of this rate has important ramifications for storage security. In this section, we will first look at the intricacy of identifying this stabilized flux from numerical simulations. We will then look at how fingering structures vary with κ , ϕ and $\tau\mathcal{D}$. We also determine the empirical relations between the long-time mass flux and these formation properties.

4.2.1. Numerical Considerations

Figure 9 shows the evolution of $F_0(t)$, the mass flux at the top boundary, for a domain of size 1 m \times 8 m. To determine whether the flux has indeed stabilized, we compute the moving average of F_0 , defined as

$$F_m(t) = \frac{1}{\Delta t} \int_{t-\Delta t/2}^{t+\Delta t/2} F_0(t') dt' \quad (18)$$

where Δt is sufficiently large that fluctuations in F_m are below 5% for the last N_s time steps at which F_m is evaluated; in this study, $N_s = 100$. We note that in our simulation, the time

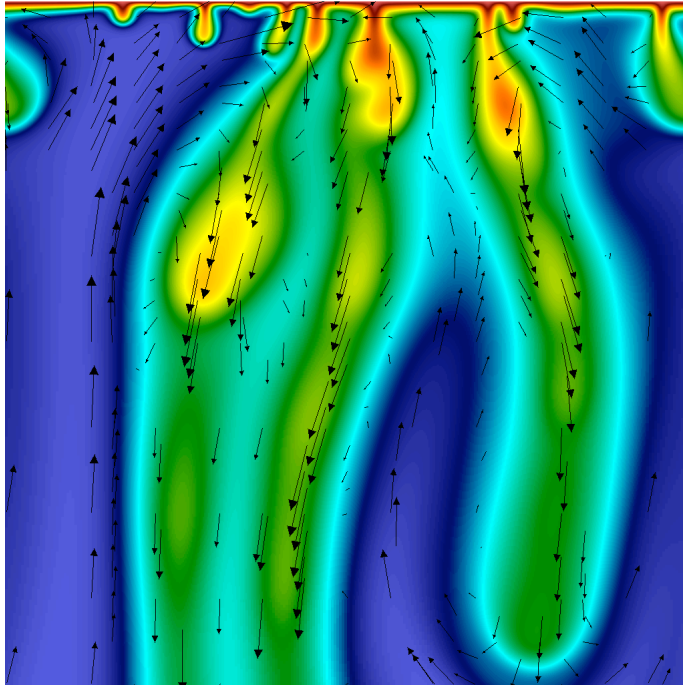


Figure 8: Component density of $\text{CO}_2(\text{aq})$ after a long time.

step is determined based on the advective CFL number which is fixed at 0.75. For different combinations of κ and ϕ , fixed N_s will lead to different values of Δt . A comparison based on fixed N_s (with fixed CFL number) instead of fixed Δt then allows us to take the scale differences in space and time into consideration. We further define the stabilized flux $\langle F_0 \rangle$ as

$$\langle F_0 \rangle = \frac{1}{\Delta T} \int_{T-\Delta T}^T F_m(t) dt \quad (19)$$

where T is the last t at which F_m is evaluated, and ΔT is chosen such that the interval $[T - \Delta T, T]$ contains N_s sample points of F_m . The fingers should be sufficiently far from the bottom of the simulation domain at time $T + \Delta t/2$. For this particular case, $\Delta t = 3.1 \times 10^6 \text{s}$, and $\langle F_0 \rangle$ is found to be $1.46 \times 10^{-6} \text{ kg/m}^2/\text{s}$; $F_m(t)$ is also shown in Figure 9.

We note that F_0 fluctuates in excess of 25% with respect to $\langle F_0 \rangle$. This is likely due to boundary effects: the domain, with a width of 1 m, can only accommodate two extended fingers. There are thus insufficient fingers to provide a good averaging for determining $\langle F_0 \rangle$. In Table 3, we increase the width of the domain and determine $\langle F_0 \rangle$, the maximum relative deviations from $\langle F_0 \rangle$ in the sample set used to compute $\langle F_0 \rangle$, and the number of fingers for domains with different widths. The fluctuation decreases with increasing width; the relative deviation of F_0 from $\langle F_0 \rangle$ for $W = 16 \text{ m}$ is about a factor of 5 smaller than the relative deviation for $W = 1 \text{ m}$. The mean also appears to converge to $1.5 \times 10^{-6} \text{ kg/m}^2/\text{s}$. This shows that having a width that can accommodate two fingers may be sufficient, but a larger width will lead to better averaging. In our subsequent simulations, the domain size will vary with the parameters used. The results are checked to ensure that the domains are sufficiently large that we have at least two extended fingers and the magnitudes of the velocities at the lower boundary is still zero (up to the prescribed solver tolerances) at the end of the simulations. The second criterion ensures that the finger tips are sufficiently far from the lower boundary.

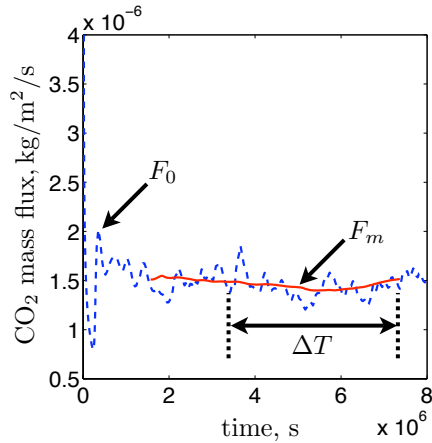


Figure 9: Variation of F_0 and F_m with time. The stabilized mass flux $\langle F_0 \rangle$ is determined based on F_m within the interval ΔT indicated in the plot. Here $\langle F_0 \rangle$ is approximately 1.50×10^{-6} kg/m²/s.

W	$\langle F_0 \rangle$, kg/m ² /s	maximum relative deviation	number of fingers
1	1.46×10^{-6}	27.0	2
2	1.48×10^{-6}	12.2	4
8	1.52×10^{-6}	7.2	8
16	1.50×10^{-6}	5.7	17

Table 3: Stabilized mass fluxes for different domain size. The deviation shown is the maximum absolute relative deviation of F_0 from $\langle F_0 \rangle$.

We next examine what effects the magnitude of the relative fluctuation has on the stabilized mass flux. Table 4 shows that there is no distinct correlation between $\langle F_0 \rangle$ and the % fluctuation in κ ; κ has a mean of 10 D, and constant $\phi = 0.3$ and $\tau\mathcal{D} = 2 \times 10^{-9}$ m²s⁻¹ are used. Furthermore, using the solution for the 0.25% fluctuation case as reference, we see that the deviations of $\langle F_0 \rangle$ for all other cases are within the 5% window that we use to determine $\langle F_0 \rangle$. Thus, we can conclude that $\langle F_0 \rangle$ does not depend on strength of the fluctuations.

4.2.2. Stabilized Mass Flux

The characteristics of the fingering phenomenon are primarily determined by the relative strength between the convective process and the diffusive process. As $\bar{\kappa}$ increases, the Darcy velocity \mathbf{u} increases as well due to (2). The convective term $\nabla \cdot \rho X \mathbf{u}$ is correspondingly larger, which diminishes the stabilizing effects of the diffusive process. Thus, more extended fingers are formed per unit width, and these fingers are in general narrower, as shown in Figure 10. On the other hand, an increase in $\bar{\phi}$ reduces the effects of convective process.

% fluctuation	$\langle F_0 \rangle$, kg/m ² /s	maximum % deviation from the 0.25% case
0.25	1.52×10^{-6}	—
0.5	1.50×10^{-6}	1.9
1	1.59×10^{-6}	4.5
2	1.53×10^{-6}	1.0
10	1.55×10^{-6}	2.1

Table 4: Stabilized mass fluxes for different levels of fluctuation.

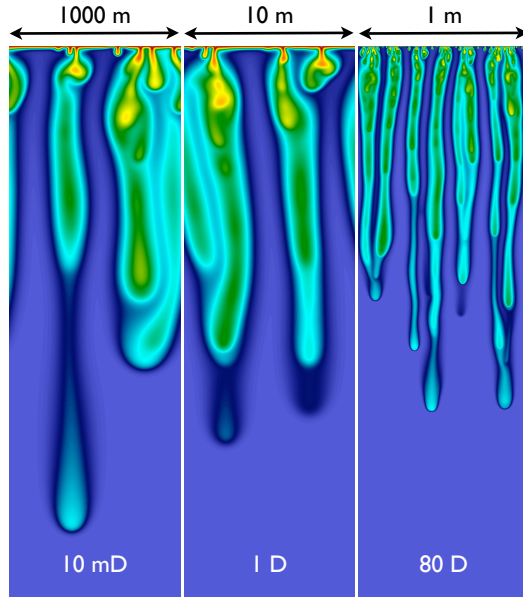


Figure 10: Density of CO_2 for $\bar{\kappa} = 10 \text{ mD}$, 1 D and 80 D . Time at which the snapshots are taken are respectively $4 \times 10^{12} \text{ s}$, $4 \times 10^8 \text{ s}$, and $4 \times 10^5 \text{ s}$.

Thus, as $\bar{\phi}$ increases, the number of fingers per unit width decreases, and the fingers become wider, as shown in Figure 11. Similarly, as $\tau\mathcal{D}$ increases, the number of fingers per unit width decreases, as shown in Figure 12.

Our convergence study in Section 4.2.1 has shown that the long-time mass flux reaches a stabilized state as we approach geological length scales. We would like to determine the empirical relations between $\langle F_0 \rangle$ and various formation properties. To determine these relations, simulations with different combinations of $\bar{\kappa}$, $\bar{\phi}$ and \mathcal{D} are performed. The ranges examined are similar to Section 4.1.2 for most cases. In the κ case, the range is $[0.01, 80] \text{ D}$. In the ϕ case, the range is reduced to $[0.05, 0.4]$ because the domain size needed to accommodate sufficient number of fingers for $\phi > 0.4$ can be quite large. Since ϕ is in general small in real aquifers, this smaller range avoids unnecessary demands on the available computational resources. In the $\tau\mathcal{D}$ case, the range we examined is $[0.5, 4] \times 10^{-9} \text{ m}^2\text{s}^{-1}$ and κ and ϕ are respectively 500mD and 0.15 . Based on Figure 13, we can conclude that $\langle F_0 \rangle$ is proportional to $\bar{\kappa}$ but does not depend on $\bar{\phi}$ and $\tau\mathcal{D}$. This shows that although a decrease in $\bar{\phi}$ or $\tau\mathcal{D}$ leads to an increase in the number of fingers per unit width, it does not imply an increase in $\langle F_0 \rangle$.

We now determine the magnitude of a dimensionless flux term based on the above results. Following [22], we scale \mathbf{u} , ρ and X by $\kappa\Delta\rho g/\mu$, $\Delta\rho$ and X_0 . The dimensionless flux F^* is then given by

$$F^* = F \left(\frac{\mu}{C_0 \kappa \Delta \rho g} \right). \quad (20)$$

Evaluating the data in Figure 13 yields $\langle F^* \rangle \approx 0.017 - 0.018$. Similar results are found in [7] where the average dimensionless dissolution rate (equivalent to $\langle F^* \rangle$) is found to be approximately 0.017 and independent of the Rayleigh number. However, due to the scaling relations used in [7], Hesse suggested that mass dissolution rate of CO_2 is given by $0.017 \frac{C_0 \kappa \Delta \rho g}{\phi \mu}$. The dependence on ϕ is again a result of scaling t by $\phi H^2/D$, where H is the characteristic length, instead of H^2/D used in [4, 5, 26]. If the latter is used, the scaling result

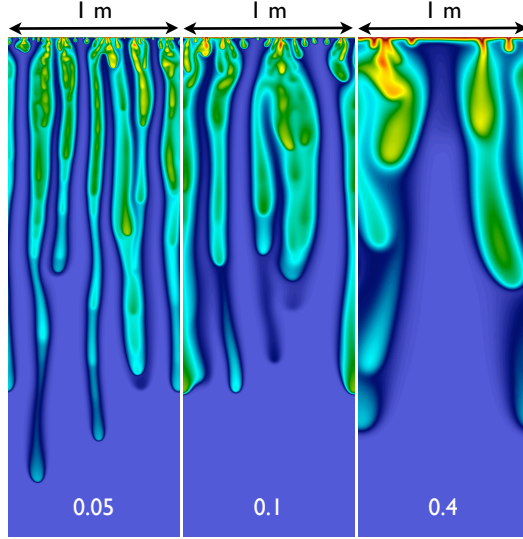


Figure 11: Density of CO_2 for $\bar{\phi} = 0.05, 0.1$ and 0.4 . Times at which the snapshots are taken are respectively 6×10^5 s, 1×10^6 s and 6×10^6 s.

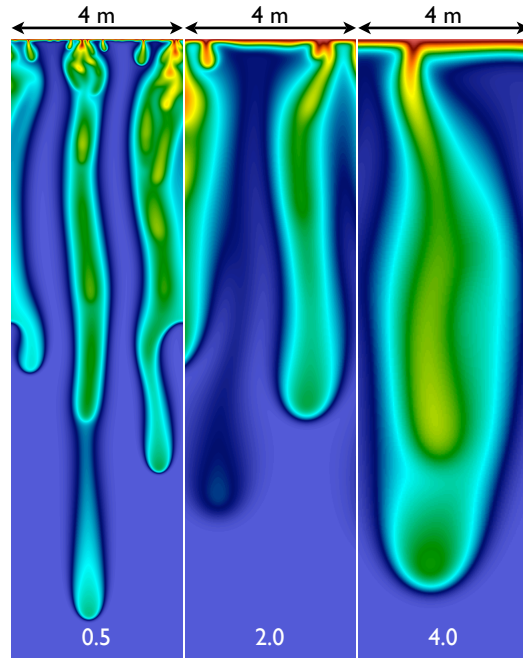


Figure 12: Density of CO_2 for $\tau\mathcal{D} = 0.5, 1$ and $4 \times 10^{-9} \text{ m}^2\text{s}^{-1}$. Times at which the snapshots are taken are respectively 2.0×10^8 s, 2.1×10^8 s and 2.6×10^8 s. Note that the solutions for the last two cases are simulated on larger domains but truncated here for comparison.

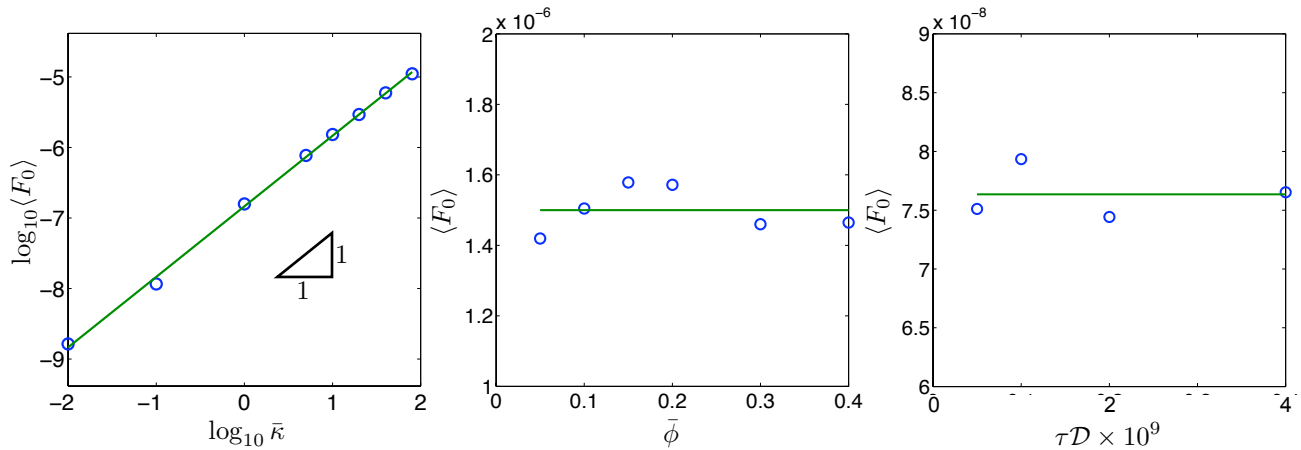


Figure 13: Variation of $\langle F_0 \rangle$ with $\bar{\kappa}$, $\bar{\phi}$ and τD .

is then consistent with the simulation results. This again shows that for scaling analysis, t should be scaled by H^2/D .

4.3. Three-Dimensional Problem

Here, we perform a three-dimensional simulation of the diffusion-convection process to determine whether the results will differ significantly from a two-dimensional simulation. Since a 3D simulation is significantly more resource intensive, we will examine only one set of hydrogeologic parameters, corresponding to the Carrizo-Wilcox aquifer in Texas; its deeper sections are very large and promising targets for CO₂ storage [15]. The Carrizo-Wilcox aquifer is modeled as having a mean permeability of 500 mD, a uniform porosity of 0.15 and uniform effective diffusivity of 2×10^{-9} m²/s; the permeability variation was modeled with a uniform random fluctuation of 1%. The simulation was performed with a parallel implementation of the AMR algorithm in 3D. The domain is of size 8 m \times 8 m \times 32 m. Four levels of grids are used, and grids at the finest level have a resolution of 1/128 m. CPU, memory and storage requirements for a simulation based on a uniform grid at the finest resolution would have been significantly larger than that required by an AMR-based method.

Figure 14 shows the velocity fields and the contour plots of the CO₂ densities for two different levels at $t = 3 \times 10^7$ s, 4.8×10^7 s and 3.8×10^8 s. At time 3×10^7 s, the isoconcentration surface resembles a rippled sheet. Velocities point upward at the crests and downward at the ridges. The downward velocities are also larger, as indicated by the larger arrows, thus facilitating the growth of fingers. As time progresses, the flow develops into a circulating flow field. Shown in the image at $t = 4.8 \times 10^7$ s is an intermediate stage of the growth where the presence of many pockets of upward and downward fluid leads to a rather complex flow pattern. The isoconcentration surface is less wavy and narrow ridges are being formed due to the merging of nascent fingers, a process driven by the velocity field. Eventually, a quasi-steady circulating flow field is obtained, as shown in the image at $t = 3.8 \times 10^8$ s. The velocity field bears close resemblance to the 2D results shown in Figure 8. However, when pockets of upward moving fluid reach the top boundary, they move outward in all directions of a horizontal plane instead of moving along a horizontal line as in the case of 2D flow. As a result, narrow ridges are formed when different pockets of the diverted fluid meet and they act as conduits for downward moving fluid; we note that the

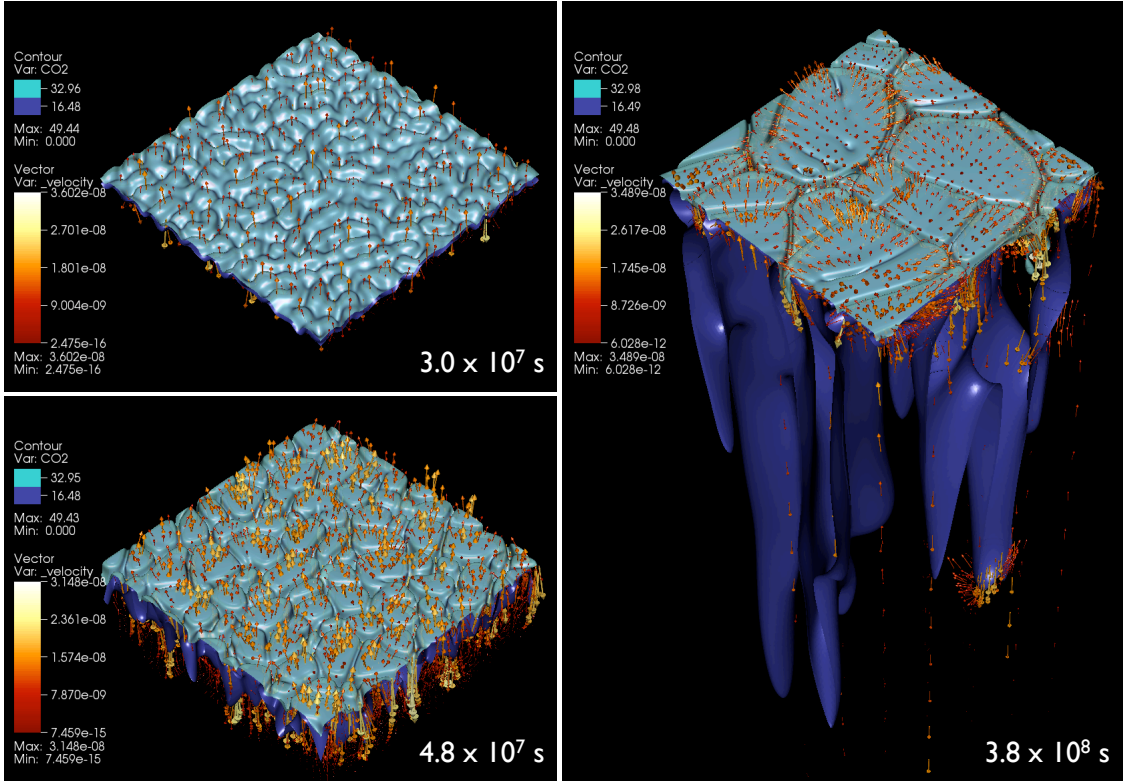


Figure 14: Evolution of the velocity fields and CO₂ densities at different times.

downward velocity is usually largest along the ridges. Here, quasi steady state refers to a state where the maximum size of the pockets stays approximately constant, but the flow pattern evolves dynamically.

In Figure 15, we show the isosurface of CO₂ concentration at $\rho X = 24 \text{ kg/m}^3$ to highlight the structure of the 3D fingers. The fingers at early time ($t = 3 \times 10^7 \text{ s}$) are approximately cylindrical in shape as one would deduce from a 2D simulation assuming the 2D fingers are similar in all directions perpendicular to the z -axis. For our discussion here, the z -axis is along the direction of the gravity, xy -plane is perpendicular to z -axis, and $z = 0$ is the top boundary. However, as time progresses, the fingers grow larger and flatter. When we compare the cross-sections of the 3D solution along the yz -plane at $3.8 \times 10^8 \text{ s}$ to the 2D solution, the differences, as shown in Figure 16, are apparent. In particular, the cross-section along $x = 4 \text{ m}$ shows a cross-section of the flat three-dimensional fingers observed in Figure 15 that cannot be deduced from a 2D simulation. This network of flat fingers is more clearly shown by the cross-sections along the xy -plane in Figure 17. The finger tips also show a less rounded profile compared to those in the 2D simulation, as shown in Figure 16. These observations suggest that while the early-time behavior can be predicted based on a 2D model, there are significant differences between the 2D and 3D fingering structures. Note that the finest level of the AMR grid is also shown in the image for $t = 3.8 \times 10^8 \text{ s}$ of Figure 15. Only a small percentage of the whole domain needs to be resolved at the finest level, leading to greater computational efficiency.

It is clear from the above that the additional degrees of freedom add significant complexity to the fingering phenomena. We next determine whether it has any appreciable influence on the integral measures that we are interested in. In Figure 18, we compare the evolution of F_0

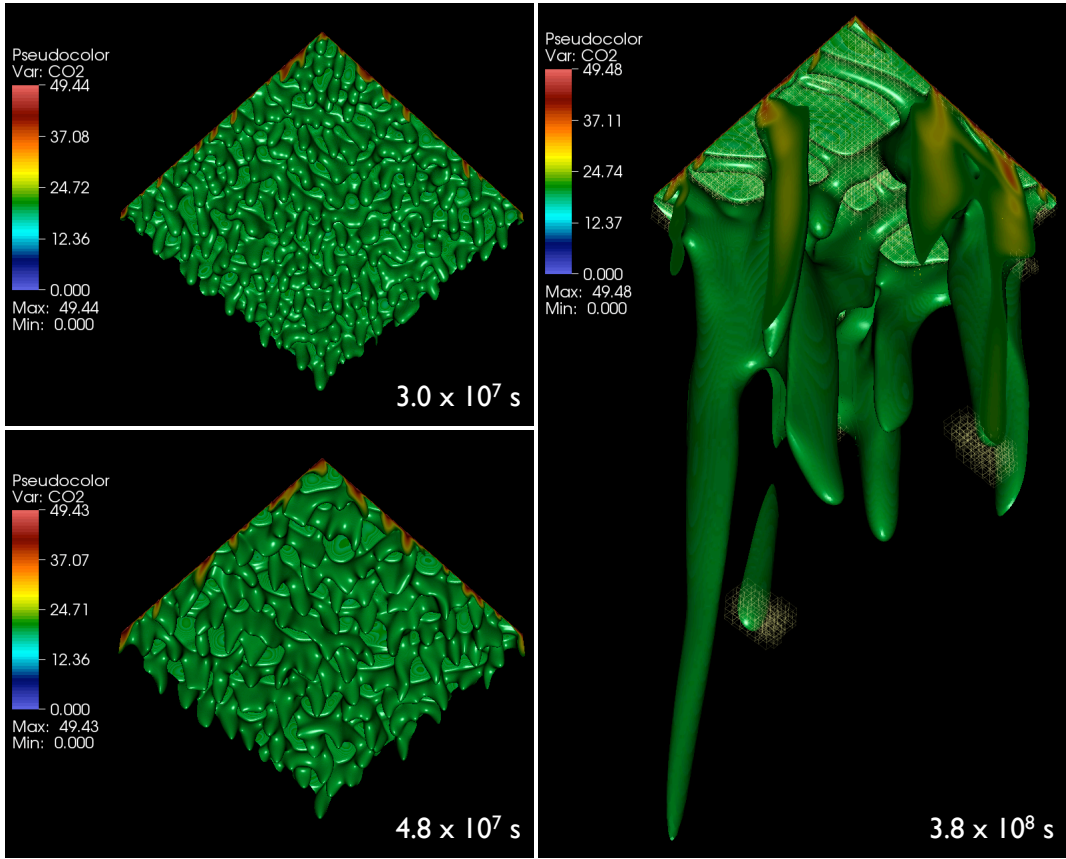


Figure 15: A view from below shows flat characteristic of the fingers. The surface corresponds to a concentration of 20 kg/m^3 . The yellow boxes shown in the viewgraph for $t = 3.8 \times 10^8 \text{ s}$ is the finest level of the AMR grid.

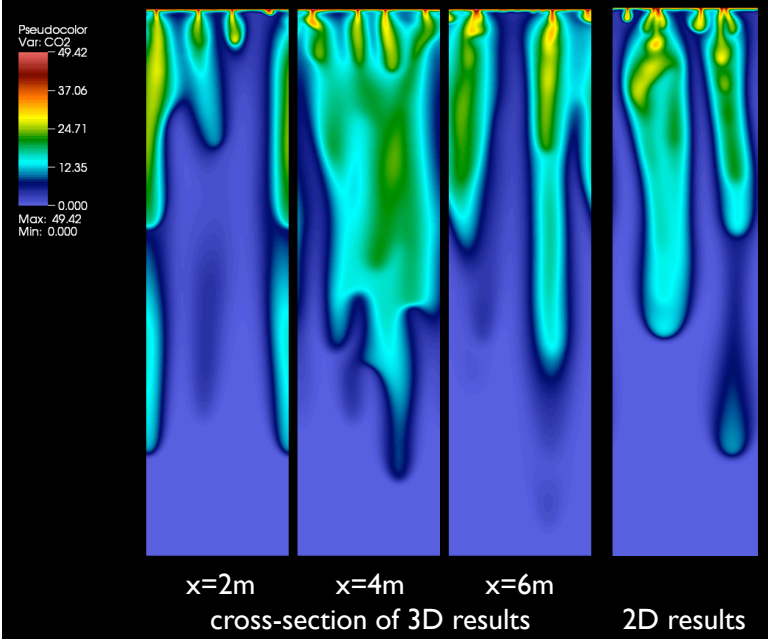


Figure 16: A comparison between cross-sections in the yz -plane of the 3D solution at $t = 3.8 \times 10^8 \text{ s}$ and a 2D solution.

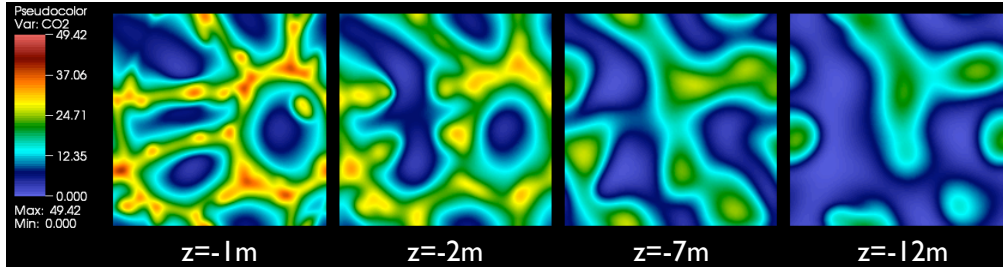


Figure 17: Cross-sections in the xy-plane of the 3D solution at $t = 3.8 \times 10^8$ s.

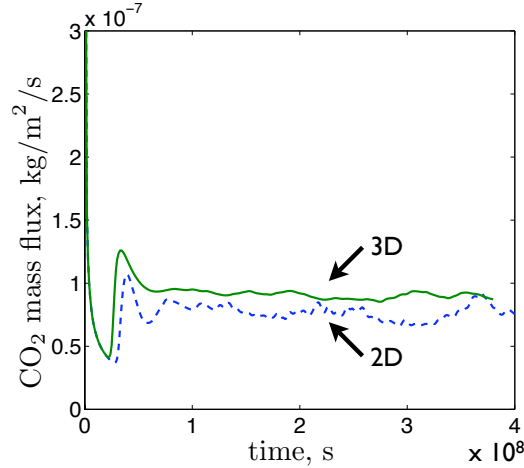


Figure 18: Comparing the results from a 2D simulation and a 3D simulation.

of a 3D simulation to a 2D simulation with the same fluid and formation parameters, and grid resolution. We obtain a somewhat smaller onset time and a higher maximum mass flux during the transient stage. The fluctuation of mass flux at long time is also smaller compared to the 2D simulation due to larger number of fingers which leads to better averaging. The stabilized mass flux is found to be 8.97×10^{-7} kg/m²/s, which is 25% higher than a comparable 2D simulation. While the difference is statistically significant, the increase is small in view of the typically large variation in permeability for geologic media. Thus the effect of additional spatial degrees of freedom on onset time and stabilized mass flux is modest.

5. Comparison to Results from TOUGH2-MP

The same problem of convective instability discussed above was simulated with a parallelized version TOUGH2-MP [28] of the general-purpose reservoir simulator TOUGH2. Initial calculations used the ECO2N fluid property module [19]. However, since the conditions in the present problem are limited to a single aqueous phase, a more efficient simulation can be obtained by using EOS7, in which the fluid is represented as a two-component mixture of H₂O and brine. We use the brine component to represent density changes in the aqueous phase from CO₂ dissolution. Numerical work is approximately proportional to NEQ^2 , where NEQ is the number of equations per grid block. Accordingly, a given problem can be solved with EOS7 ($NEQ = 2$) in less than half the time required with ECO2N ($NEQ = 3$). Our test calculations have confirmed excellent agreement between simulations using EOS7 and ECO2N.

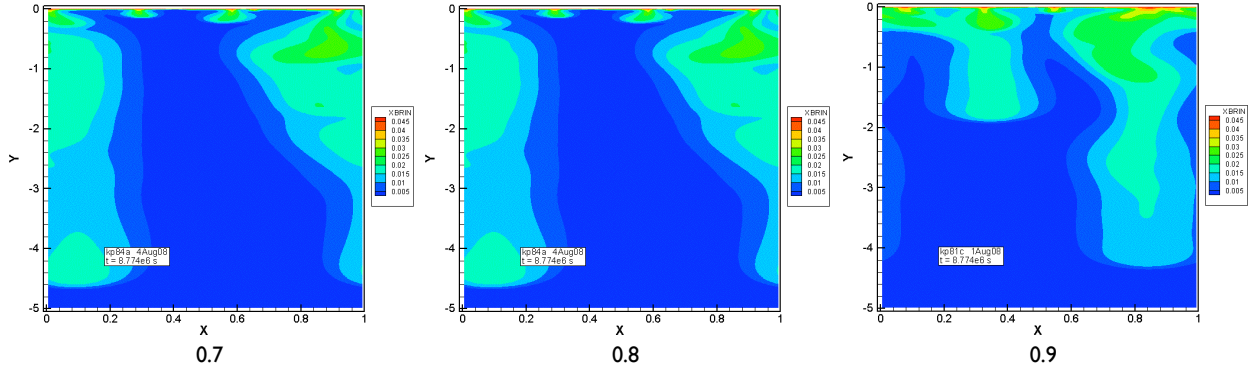


Figure 19: Simulated distribution of dissolved CO_2 after 101.6 days for three different random number seeds to generate permeability heterogeneity (given at the bottom of each plot). Note the different horizontal and vertical scales.

To achieve results with “small” space discretization errors, we experimented with different domain sizes and grid resolutions. We found a domain of width $W = 1$ m, height $H = 5$ m, and a vertical grid resolution of 1 mm near the top boundary, which was gradually coarsened going downward, to be sufficient. Horizontal grid resolution was 10 mm, and the total number of grid blocks was 52,300.²

5.1. Results

The convective pattern shows similar features to those seen in the adaptive grid simulations discussed previously, including fingering convection, merging and pinch-off of fingers, and continuous generation of new fingers as older ones grow. As an example, Figure 19 shows convective patterns for three different random number seeds after a time of 101.6 days. The resolution of features is somewhat inferior in comparison to the adaptive gridding, Figure 8. Specifics of the convective activity are very sensitive to small problem variations, but we observe that integral measures of the process, such as onset time of convection, and long-term behavior of the CO_2 mass flux carried by the convection, are quite robust to modest changes in problem parameters. Indeed, for the three cases with different random permeability fields shown in Figure 19, onset times of convection are identical, and long-term stabilized fluxes show random fluctuations of $\pm 15\%$ about the same mean of approximately 1.3×10^{-6} kg/m²/s.

We explored the sensitivity of the onset time for convection to the random perturbations applied to the medium. Figure 20 shows that the onset time for convection decreases with increasing strength of the applied perturbation of the medium. Porosity perturbations are seen to be more effective in triggering convective instability than permeability perturbations. These results are consistent with the results in Section 4.1.2, as shown in Figure 6.

A comparison calculation with a perfectly homogeneous medium yields a substantially larger onset time, as in this case convective instability arises only from numerical roundoff. The onset times obtained from TOUGH2-MP simulations are around $6 - 9 \times 10^4$ s, about a factor 3 smaller than obtained with the adaptive algorithm. At a nominal onset time of

²Simulations presented here were performed on a Dell T5400 dual quad core computer with a total of 8 cores, and in most cases 16 processes were run (two per processor), as this was found to reduce total execution time compared to running 8 processes. Depending on grid resolution and simulation time, individual runs typically took from 1/2 to 4 hours.

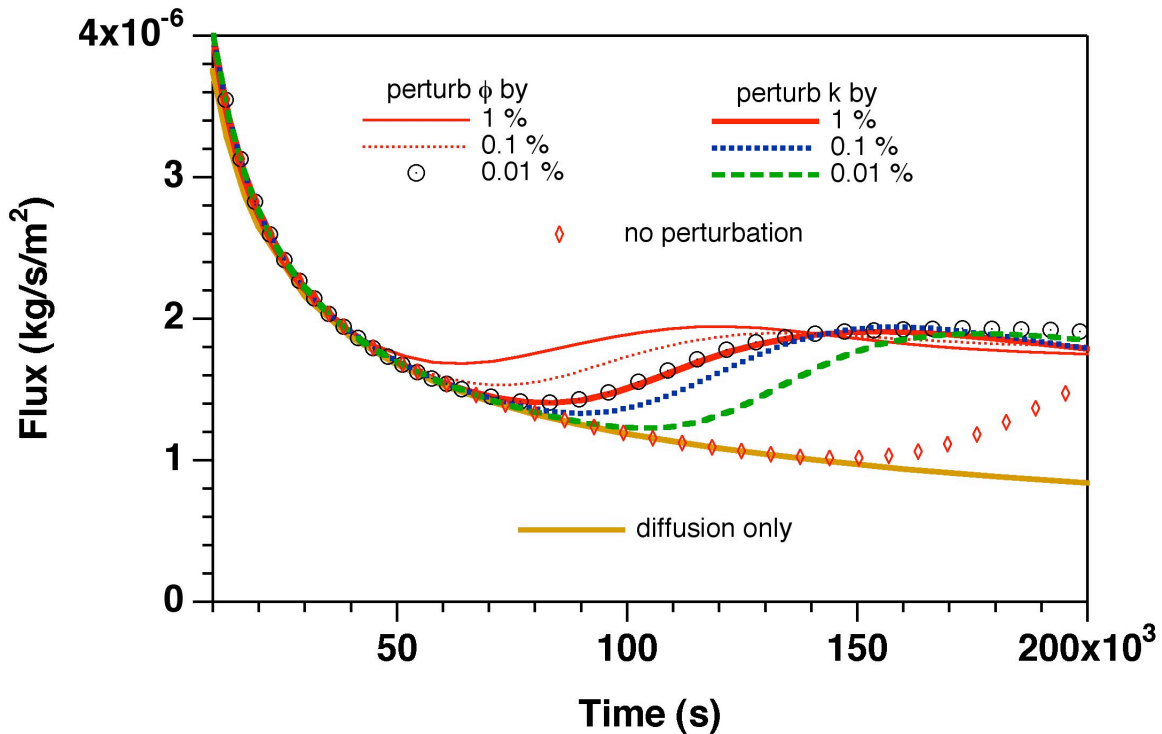


Figure 20: Simulated CO₂ fluxes at the top boundary at early times, for different random perturbations of the porosity or permeability field.

7.5×10^3 s, the thickness of the diffusive boundary layer is 12.2 mm, which should be well resolved with our 1 mm grid resolution. Potential reasons for the discrepancy are similar to the reasons given for the discrepancy in c_0 discussed in Section 4.1.2.

The convective CO₂ flux at the top is equal to the CO₂ dissolution rate per unit area. Due to the partially chaotic nature of the convection process, this rate fluctuates, but the fluctuations are modest in size, and fluxes stabilize at 1.3×10^{-6} kg/m²/s ($\pm 15\%$), regardless of how the instability was triggered (Figure 21). This is approximately 13% smaller than the value obtained from the adaptive gridding simulations. This is likely due to the higher resolution achieved by the adaptive gridding simulations, which allow fine-scale convective behavior, including those away from the top boundary, to be resolved.

We also performed simulations with different boundary conditions at the sides and bottom of the domain, such as no flow conditions on the sides, and constant pressure conditions on the bottom. Onset times for convection and long-term stabilized fluxes were found to be insensitive to boundary conditions. A more extensive account of TOUGH2 analyses of the dissolution-diffusion-convection process is available in a laboratory report [20].

6. Conclusion

High-resolution two-dimensional simulations of the diffusion-convection process in CO₂ sequestration were performed using a block structured adaptive mesh refinement method. Numerical aspects of the simulations were examined and the short and long term behaviors of the process are examined.

We found that although details of the convection process are chaotic in nature, integral measures, such as the onset time of convection, and the long-term CO₂ mass flux associated

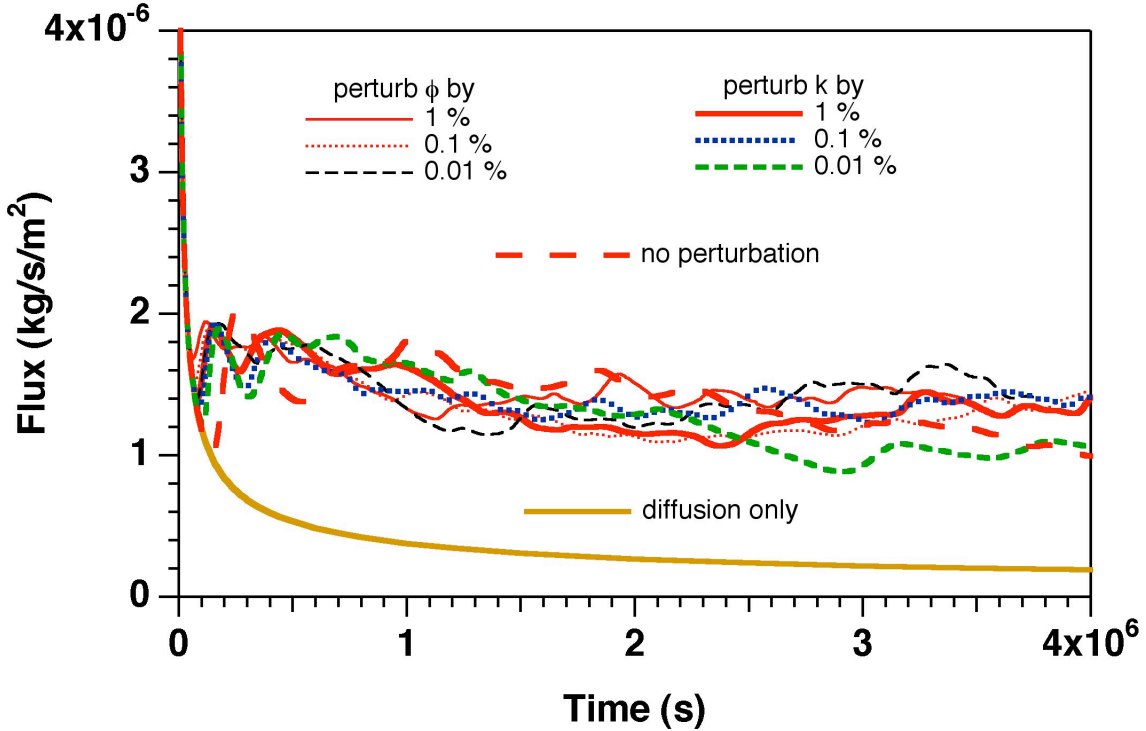


Figure 21: Longer-term behavior of simulated CO₂ fluxes at the top boundary.

with the convective activity, are robust and insensitive to modest problem variations. At short time, the onset time of convection follows the prediction of linear stability analysis. The constant c_0 in (17) for onset time is found to be in the range of 1000-5000 and is dependent on the level of fluctuation in the formation properties. It is of the same order of magnitude as that reported in [20] and any discrepancy can be attributed to differences in the details of the simulation parameters. There are however large variations in the value of c_0 reported in the literature. These variations can usually be attributed to differences in the models used to describe the diffusion-convection process, the criteria by which the onset time is determined, and the levels or forms of fluctuations used in the simulations.

At long time, the CO₂ mass flux reaches a stabilized state that approaches a constant value at space and time scales of interest for geological storage of CO₂. In particular, we show that the long term behavior is convection-dominated and depends only on the mean value of the permeability. It also does not depend on the level of fluctuation. These empirical observations suggest that we can model the behavior of the process on geological time and space scales using a simplified model. Let the formation properties be uniform and given by the mean values. Then the mass conservation equation for CO₂ given by (1) can be expressed as

$$\frac{\partial \bar{\phi} \rho X_1}{\partial t} + \nabla \cdot F = \nabla \cdot \bar{\phi} \tau \mathcal{D} \rho \nabla X_1, \quad (21)$$

where $F = \rho X_1 \mathbf{u}$ and $\mathbf{u} = -\frac{\bar{\kappa}}{\mu} (\nabla p - \rho \mathbf{g})$. The linear relation between $\langle F_0 \rangle$ and $\bar{\kappa}$ suggests that the dominant mechanism by which CO₂ is transported downward is convective in nature and can be efficiently modeled using the mean values of κ and ϕ . In addition, since $\langle F_0 \rangle$ does not depend on $\tau \mathcal{D}$, we can further approximate the divergence condition (9) by

$$\nabla \cdot \mathbf{u} = 0. \quad (22)$$

Since the top boundary is impermeable, we must model the influx of $\text{CO}_{2(\text{aq})}$ at the top boundary explicitly by imposing the boundary condition

$$\bar{\phi}\tau\mathcal{D}\rho\nabla X_1 = \langle F_0 \rangle, \quad (23)$$

at the top boundary, with a corresponding condition for $\bar{\phi}\tau\mathcal{D}\rho\nabla X_2$ so that the net mass flux is zero.

The divergence condition (22), the conservation equation (21) and the boundary condition (23) then constitute a simplified model that is relevant on geological scales where the complex convective pattern at small scales can be approximated by a uniform convective flux. Since the model depends only on the mean values of κ , ϕ , and $\tau\mathcal{D}$, we can avoid the need to resolve the fluctuations that lead to the fingering phenomenon. Thus, we do not need to take the diffusive layer, which is small relative to the geological length scale, and the onset time, which is again small relative to the geological time scale, into consideration. When used as a subgrid model, this model can potentially simplify the inclusion of the dissolution-diffusion-convection process in a large-scale flow simulation of carbon sequestration. The use of this model as a subgrid model in a large-scale multiphase flow simulation of carbon sequestration will be examined in future work.

A detailed three-dimensional simulation shows that the added degrees of freedom add significant complexity to the fingering phenomena. However, the changes in the integral measures, i.e. the onset time and stabilized mass flux, are modest when compared to the two-dimensional simulations. Results from the two-dimensional simulations are also compared to results from TOUGH2-MP and good agreement is obtained.

7. Acknowledgement

Support for this work was provided by the Applied Mathematics Research Program and the Office of Basic Energy Sciences of the U.S. Department of Energy under contract DE-AC02-05CH11231. This research used resources of the National Energy Research Scientific Computing Center and the Lawrence computational cluster resource provided by the LBNL's IT Division, both of which are supported by the Office of Science of the U.S. Department of Energy under the same contract.

Appendix

A. Scaling Study

To measure the parallel performance of the algorithm, we use a weak scaling study based on a replicated problem strategy as discussed in [1]. We consider a three-dimensional three-component two-phase system with a layered permeability function. A pressure drop is applied along the x -direction and gravity is ignored. By replicating the problem in the y and z directions, we are able to scale the problem size without modifying the problem characteristics, particularly with regard to how adaptive criteria and grid generation impact the overall problem. In Figure 22, we present scaling data compared to ideal behavior for a range of processors from 256 to 2048. We observe a small deviation from the ideal scaling, which is primarily attributable to increases in the time spent in the elliptic solver.

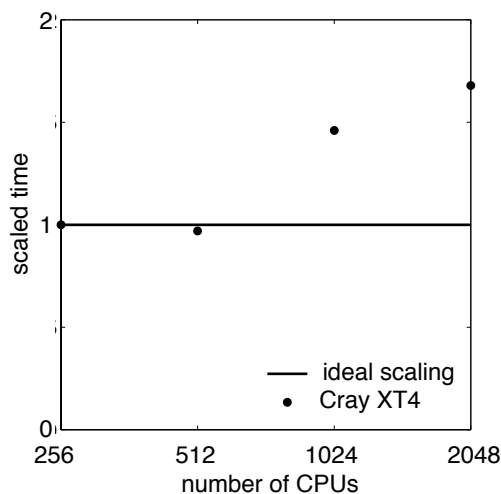


Figure 22: Parallel performance of the adaptive algorithm based on weak scaling.

References

- [1] P. Colella, J. B. Bell, N. Keen, T. Ligocki, M. J. Lijewski, and B. van Straalen. Performance and scaling of locally-structured grid methods for partial differential equations. *Journal of Physics: Conference Series*, 78:012013, 2007.
- [2] J. Douglas Jr., D. Frías, N. Henderson, and F. Pereira. Simulation of single-phase multicomponent flow problems in gas reservoirs by Eulerian-Lagrangian techniques. *Transport in Porous Media*, 50:307–342, 2002.
- [3] J. Ennis-King and L. Paterson. Coupling of geochemical reactions and convective mixing in the long-term geological storage of carbon dioxide. *International Journal of Greenhouse Gas Control*, 1(1):86–93, 2007.
- [4] J. P. Ennis-King and L. Paterson. Role of convective mixing in the long-term storage of carbon dioxide in deep saline formations. *SPE J.*, 10(3):349–356, 2005. SPE-84344-PA.
- [5] J. P. Ennis-King, I. Preston, and L. Paterson. Onset of convection in anisotropic porous media subject to a rapid change in boundary conditions. *Physics of Fluids*, 17(8):084107, 2005.
- [6] J. Gounot and J. P. Caltagirone. Stabilité et convection naturelle au sein d’une couche poreuse non homogène. *International Journal of Heat and Mass Transfer*, 32(6):1131 – 1140, 1989.
- [7] M. A. Hesse. *Mathematical Modeling and Multiscale Simulation for CO₂ Storage in Saline Aquifers*. Ph.D., Dept. of Energy Resources Engineering, Stanford University, May 2008.
- [8] J. J. Hidalgo and J. Carrera. Effect of dispersion on the onset of convection during CO₂ sequestration. *Journal of Fluid Mechanics*, 640(-1):441–452, 2009.
- [9] J. J. Hidalgo, J. Carrera, and A. Medina. Role of salt sources in density-dependent flow. *Water Resour. Res.*, 45, 2009.

- [10] K. Johannsen. On the validity of the Boussinesq approximation for the Elder problem. *Computational Geosciences*, 7(3):169–182, 2003.
- [11] J. W. Johnson, J. J. Nitao, C. I. Steefel, and K. G. Knaus. Reactive transport modeling of geologic CO₂ sequestration in saline aquifers: the influence of intra-aquifer shales and the relative effectiveness of structural, solubility, and mineral trapping during prograde and retrograde sequestration. In *Proceedings of first national conference on carbon sequestration*, Washington, DC, 2001.
- [12] T. J. Kneafsey and K. Pruess. Laboratory flow experiments for visualizing carbon dioxide-induced, density-driven brine convection. *Transport in Porous Media*, 2009.
- [13] A. Landman and R. Schotting. Heat and brine transport in porous media: the Oberbeck-Boussinesq approximation revisited. *Transport in Porous Media*, 70(3):355–373, 2007.
- [14] E. Lindeberg and D. Wessel-Berg. Vertical convection in an aquifer column under a gas cap of CO₂. *Energy Conversion and Management*, 38(Supplement 1):S229 – S234, 1997.
- [15] J. P. Nicot. Evaluation of large-scale CO₂ storage on fresh-water sections of aquifers: An example from the Texas gulf coast basin. *Int. J. Greenhouse Gas Control*, 2:583–593, 2008.
- [16] D. A. Nield. General heterogeneity effects on the onset of convection in a porous medium. In *Emerging Topics in Heat and Mass Transfer in Porous Media*, pages 63–84, 2008.
- [17] G. S. H. Pau, A. S. Almgren, J. B. Bell, and M. J. Lijewski. A parallel second-order adaptive mesh algorithm for incompressible flow in porous media. *Phil. Trans. R. Soc. A*, 367:4633–4654, 2009.
- [18] K. Pruess. The TOUGH codes – a family of simulation tools for multiphase flow and transport processes in permeable media. *Vadose Zone J.*, 3:738–746, 2004.
- [19] K. Pruess and N. Spycher. ECO2N – a fluid property module for the TOUGH2 code for studies of CO₂ storage in saline aquifers. *Energy Conversion and Management*, 48(6):1761–1767, 2007.
- [20] K. Pruess and K. Zhang. Numerical modeling studies of the dissolution-diffusion-convection process during CO₂ storage in saline aquifers. Technical Report LBNL-1243E, Lawrence Berkeley National Laboratory, Calif., 2008.
- [21] D. A. S. Rees, A. Selim, and J. P. Ennis-King. The instability of unsteady boundary layers in porous media. In *Emerging Topics in Heat and Mass Transfer in Porous Media*, pages 85–110, 2008.
- [22] A. Riaz, M. Hesse, H. A. Tchelepi, and F. M. Orr. Onset of convection in a gravitationally unstable diffusive boundary layer in porous media. *Journal of Fluid Mechanics*, 548:87–111, 2006.
- [23] F. Tewes and F. Boury. Formation and rheological properties of the supercritical CO₂-water pure interface. *J. Phys. Chem. B*, 109(9):3990–3997, 2005.

- [24] G. J. Weir, S. P. White, and W. M. Kissling. Reservoir storage and containment of greenhouse gases. In K. Pruess, editor, *Proceedings of the TOUGH Workshop 1995*, pages 233–238, Berkeley, CA, 1995.
- [25] G. J. Weir, S. P. White, and W. M. Kissling. Reservoir storage and containment of greenhouse gases. *Transport in Porous Media*, 23:37–60, 1996.
- [26] X. Xu, S. Chen, and D. Zhang. Convective stability analysis of the long-term storage of carbon dioxide in deep saline aquifers. *Advances in Water Resources*, 29(3):397 – 407, 2006.
- [27] C. Yang and Y. Gu. Accelerated mass transfer of CO₂ in reservoir brine due to density-driven natural convection at high pressures and elevated temperatures. *Industrial & Engineering Chemistry Research*, 45(8):2430–2436, 2006.
- [28] K. Zhang, Y. Wu, and K. Pruess. User’s guide for TOUGH2-MP – a massively parallel version of the TOUGH2 code. Technical Report LBNL-315E, Lawrence Berkeley National Laboratory, Calif., 2008.